THE ASTROPHYSICAL JOURNAL, 364:123–135, 1990 November 20

INTERSTELLAR PROPAGATION EFFECTS AND THE PRECISION OF PULSAR TIMING

R. S. FOSTER
Astronomy Department and Radio Astronomy Laboratory, University of California at Berkeley

AND

J. M. CORDES
Astronomy Department and National Astronomy and Ionosphere Center, Cornell University
Received 1990 March 9; accepted 1990 May 18

ABSTRACT

Interstellar propagation effects induced by electron-density turbulence limit the precision of pulsar timing. We study three distinct arrival time perturbations that are associated with propagation through the ionized component of the interstellar medium. One is due to variations in the electron-column density while angle-of-arrival variations cause the other two. The three effects have different frequency scalings as well as different time dependences for electron-density fluctuations having a wide distribution of length scales. We assess the feasibility of removing propagation effects by analyzing multi-frequency timing measurements. Maximization of the signal-to-noise ratio from weak pulsars forces observations toward low frequencies where the amplitudes of interstellar propagation effects increase. We examine in detail the arrival times from simulated PSR 1937+21 data and draw the following conclusions: (1) for a Kolmogorov power-law spectrum, the arrival time errors are dominated by dispersion measure variations at radio frequencies above several hundred Megahertz; (2) dual-frequency observations can be used to remove dispersion measure variations to obtain sub-microsecond residuals; (3) the remaining residuals are highly correlated with the angle-of-arrival variations; (4) fitting for a non-λ^2 term does improve the final residuals, although it does not appear to improve the measurement of the astrometric terms of proper motion and parallax; and (5) frequent sampling with a small antenna is better for allowing removal of propagation effects and measuring proper motion and parallax in timing data than coarse sampling with a larger antenna (when the number of observations with equal time and bandwidth balances the difference in antenna gain). Simulated parallax measurements are fit within 25% of the "true" value through a turbulent phase screen along only three lines of sight: toward pulsars 1620−26, 1855+09, and 1957+20.

Subject headings: interstellar: matter — pulsars — turbulence

I. INTRODUCTION

Perturbations intrinsic to the pulsar, propagation delays of radio signals through the interstellar medium, and instrumental effects limit the precision of pulsar timing (Rickett 1977; Armstrong 1984; Blandford, Narayan, and Romani 1984; Cordes, Pidwerbetsky, and Lovelace 1986; Cordes, Foster, and Backer 1990). At ~ 1 GHz propagation effects become important at the microsecond level of timing accuracy and hence are most important for the timing of millisecond pulsars. Our ability to time millisecond pulsars at the submicrosecond level over time intervals exceeding one year will determine the ultimate utility of these pulsars as clocks and as probes of inertial frame perturbations.

In this paper we focus on interstellar propagation effects. A simulation of the propagation effects on a pulsar signal has been developed to study how multifrequency data can be used to derive times of arrival that are corrected for propagation perturbations. A phase screen is used to generate pseudo–pulse arrival times that are perturbed by turbules in the electron density. Dispersion and refraction from these turbules have been discussed by several authors (Lovelace 1970; Armstrong 1984; Blandford, Narayan, and Romani 1984; Cordes, Pidwerbetsky, and Lovelace 1986).

The basic assumption of this model is that the electron density spectrum can be approximated as a power law

$$P_{\delta n_e}(q) = C_N^2 q^{-\alpha}, \quad q_O \leq q \leq q_I , \tag{1.1}$$

where q is the fluctuation frequency, q_O and q_I are the low- and high-frequency cutoffs respectively, C_N^2 measures the amplitude of the power spectrum, and α is the spectral index (see Fig. 1). Evidence from studies of interstellar scintillation, temporal broadening, angular broadening, and angular-wandering point to the fact that the electron-density power spectrum is very close to being Kolmogorov in form, $\alpha = 11/3$ (Lee and Jokipii 1976; Cordes, Weisberg, and Boriakoff 1985; Goodman and Narayan 1985; Wilkinson *et al.* 1988; Gwinn *et al.* 1988*a*, *b*; Spangler and Cordes 1988; Cordes *et al.* 1990).

The turbulent length scales of interest that produce the arrival time perturbations in the simulation cover the "refractive" regime from 10^{11} and 10^{14} cm. Therefore our simulation performs ray tracing in the geometrical optics regime from irregularities that are much larger than the relevant Fresnel scale. In the interstellar medium, diffraction also occurs, but the resultant time of arrival (TOA) perturbations occur on time scales ~ 100 s, which we are not interested in modeling.[1] Consequently, the length scales that we need to model cover a much smaller range than if we were to consider both diffraction and refraction. The diffractive angle $\theta_d = 2(c/\pi D \Delta\nu)^{1/2}$, where D is the pulsar distance, and $\Delta\nu$ is the scintillation bandwidth. We define $l_d \equiv 1/k\theta_d$ as the diffraction

[1] Note, however, that the diffractive scintillation induced errors in arrival times will be statistically independent between observing sessions spaced by more than ~ 1 hr.

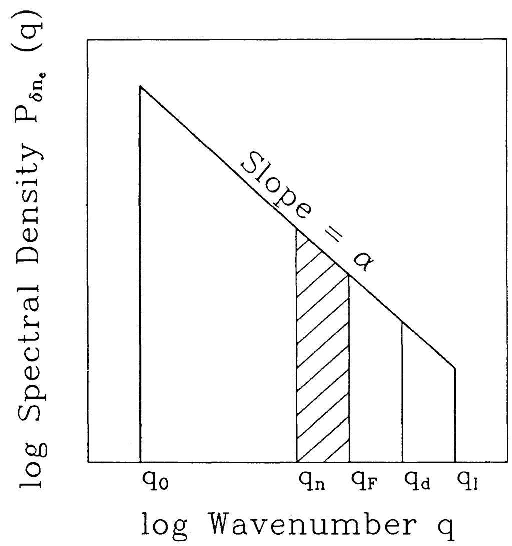

FIG. 1.—A schematic drawing shows the spectral density function $P_{\delta n_e}(q)$ vs. wavenumber on a log-log scale. The low- (outer scale) and high- (inner scale) wavenumber cutoffs are given by q_O and q_I. The diffraction wavenumber q_d, the Fresnel wavenumber q_F, and the smallest wavenumber in the simulated screen q_n are shown. The slope of the power spectrum is given as α (see eq. [1.1]). The simulation generates the power spectrum in the range from q_n up to q_F. The mean amplitude of the power spectrum scales from the diffraction wavenumber q_d set by measurements of the diffraction bandwidth or diffraction time scale.

length scale, where $k = 2\pi/\lambda$ is the wavenumber, $l_F \equiv (\lambda D/2\pi)^{1/2}$ as the Fresnel scale, and $l_r = l_F^2/l_d$ as the characteristic refraction scale. The sample interval in the screen plane Δx may be chosen to satisfy

$$l_d \ll l_F \leq \Delta x \ll l_r \, . \tag{1.2}$$

We implicitly assume that the strong scattering regime applies, in which $l_d \ll l_F$. Somewhat arbitrarily, but conveniently, we choose Δx to be

$$\Delta x = V_\perp \times \text{one day} = 10^{11.9} \text{ cm} \left(\frac{V_\perp}{100 \text{ km/s}^{-1}}\right) . \tag{1.3}$$

This sample interval is typically 10 times larger than the Fresnel scale, 10^2 times smaller than the refraction scale, and 10^3 times larger than the diffraction scale. The actual scaling equations used in the simulation are discussed in § IV.

We adopt a one-dimensional phase screen as a convenient model for studying the properties of interstellar turbulence. Since we are not examining the intensity response of the pulsar to the perturbing screen the one-dimensional simulation is a good approximation. The amplitude of refractive perturbations is reproduced by the thin screen model to within a factor of ~ 2 of those from an extended medium (Romani, Narayan, and Blandford 1986; Frehlich 1988). In addition, the location of the screen strongly affects the scintillation patterns. For our work we have assumed that a single screen is located at a distance $D_s = D/2$, where D is the pulsar distance. This produces the largest path length although not necessarily the largest refraction angle. In the case of a one-dimensional phase screen, $\alpha = 8/3$ for a Kolmogorov spectrum. The electron density fluctuations perturb the phase of electromagnetic waves proportional to the electron-column density (as a function of the transverse scale).

In this paper the results of the simulation are presented and discussed. Section II presents the arrival time model we use to generate pseudo–arrival times. We discuss the three main interstellar propagation delays in § III, while in § IV the principles used to generate the interstellar scattering delays on the pulse arrival times are developed. The pseudo–timing data are fitted according to methods summarized in § V for observing parameters similar to those encountered for the millisecond pulsar 1937+21. In § VI, results are presented for the other known millisecond pulsars. A structure function analysis is applied to the timing data and compared to the original screen in § VII. The possibility of observing a strong refractive event (Fiedler *et al.* 1987) in pulsar timing data is addressed in § VIII. In § IX we present the conclusions with guidelines on the minimum requirements for successfully removing the interstellar turbulence effects from a long-term, millisecond pulsar timing data set.

II. ARRIVAL TIME MODEL

The simulation reproduces the pulsar timing process by accounting for the spin-down of the pulsar and the motion of the Earth around the Sun. The turbulent-phase screen perturbs the arrival times, and hence affects the fitting to arrival time data that is done to determine intrinsic and astrometric parameters. A formal expression for the arrival of the Nth pulse at time t_0 corrected to the solar system barycenter at time t_s can be given as

$$\begin{aligned} t_s = {} & t_0 + NP_0 + \frac{1}{2} N^2 \dot{P}_0 P_0 \\ & + \frac{1}{c}(\boldsymbol{r_E} \cdot \hat{\boldsymbol{n}}') + \frac{1}{c} \boldsymbol{r_E} \cdot [(\hat{\boldsymbol{n}} - \hat{\boldsymbol{n}}') + \boldsymbol{\mu}_p(t - t_0)] \\ & + \frac{1}{2} \frac{r_E^2}{cD} [1 - (\hat{\boldsymbol{r}}_E \cdot \hat{\boldsymbol{n}})^2] \\ & + \Delta t_r + \frac{e^2 \langle DM \rangle}{2\pi mc} \nu_b^{-2} + \delta t_{DM} + \delta t_{\text{geo}} + \delta t_{bary} \, . \end{aligned} \tag{2.1}$$

In equation (2.1) P_0 is the pulsar spin period at the epoch t_0 in the reference frame of the solar system barycenter. The first derivative of the rotational period is given as $\dot{P}_0$. The unit vector between the solar system barycenter and the pulsar's true position on the sky is $\hat{\boldsymbol{n}}$, while the assumed position is $\hat{\boldsymbol{n}}'$, the proper motion is $\boldsymbol{\mu}_p$, and the pulsar's distance is D. The vector between the observatory and the solar system barycenter is $\boldsymbol{r_E}$. The terms in the first line of equation (2.1) describe the spin of the pulsar and its deceleration, while the second and third line describe contributions due to the correction to the barycenter, positional uncertainties, proper motion, and parallax. The fourth line contains the relativistic clock correction and plasma propagation perturbations, including the total dispersion delay. The mean dispersion measure used to correct the arrival times to infinite frequency is $\langle DM \rangle$ (see § III).

The observed radio frequency ν is corrected for the doppler shift associated with the Earth's velocity $\boldsymbol{v_E}$ by

$$\nu_b = \nu \left[1 - \frac{(\hat{\boldsymbol{n}} \cdot \boldsymbol{v_E})}{c} \right]^{-1} . \tag{2.2}$$

The relativistic clock correction Δt_r accounts for the time dilation and gravitational redshift from the changing gravitational potential of the solar system around the Earth's orbit (Blandford and Teukolsky 1976). The arrival time accuracy can be predicted to a small fraction of a microsecond using a solar system ephemeris to apply topocentric to barycentric corrections. In this simulation we assume that the relativistic correction, ephemeris correction, and mean dispersion delay have all been removed to an accuracy of 100 ns. Both the ephemeris and relativistic clock terms are neglected in our model. We would use the same model to include them as well as remove them from the pseudo data.

Additional effects that should be added to the right-hand side of equation (2.1) include (1) white noise due to radiometer noise and pulse phase jitter; (2) statistical errors associated with diffractive interstellar scintillations; (3) correlated errors due to intrinsic rotation fluctuations ("timing noise"); (4) pulsar precessional effects; (5) drifts in the Earth based atomic time standard; (6) uncertainties in the planetary ephemeris; (7) possible propagation effects associated with a stochastic background of gravitational waves; and (8) the effects of interplanetary scintillation, particularly at small solar elongations. Effects (1) and (2) are included in a joint white-noise term that is an adjustable parameter of the simulation. The other effects, which combine to give correlated time of arrival perturbations, are unmodeled in our simulation but are presumed to become evident in real data after removal of the interstellar propagation effects.

III. THE INTERSTELLAR PLASMA PROPAGATION TERMS

The plasma propagation effects are due to phase perturbations imposed by the ionized component of the interstellar medium and are in accordance with the cold plasma dispersion relation. Cordes, Foster, and Backer (1990) show that birefringence and finite temperature effects are negligible. We model the phase perturbation using a one-dimensional thin screen approximation:

$$\phi(x) = -\lambda r_e \int_0^{\Delta z} dz' \delta n_e(x, z') , \tag{3.1}$$

where r_e is the classical electron radius, λ is the wavelength, $\delta n_e(x, z)$ is the amplitude of the electron-density fluctuations, x is the transverse scale along the screen, and Δz is the screen thickness.

At most frequencies the dominant perturbation is due to changes in dispersion measure; see the third to last term in equation (2.1). The *change* in time perturbation over a time τ is

$$\delta t_{DM}(\tau) = (kc)^{-1}[\phi(x) - \phi(x + b)]_{b=V_\perp \tau} . \tag{3.2}$$

We assume that the turbulence is "frozen," and the screen and the pulsar are moving with respect to each other at the transverse velocity $V_\perp$.

The other two plasma terms in equation (2.1) are related to angle-of-arrival (AOA) variations. The refraction angle in the geometrical optics approximation is

$$\theta_r(x) = k^{-1} \frac{\partial \phi(x)}{\partial x} . \tag{3.3}$$

We consider the screen to be at distance D_s from the Earth. The *observed* angular perturbation is a factor $(1 - D_s/D)$ smaller than the refraction angle θ_r. Angle-of-arrival variations produce a geometrical delay caused by the increased path length:

$$\delta t_{\rm geo}(\tau) = \left[\frac{D_s(1 - D_s/D)}{2c}\right][\theta_r^2(x) - \theta_r^2(x + b)]_{b=V_\perp \tau} . \tag{3.4}$$

Angle-of-arrival variations also induce an error in the estimated barycentric arrival time, which is calculated from the topocentric arrival time, using an assumed position for the pulsar. The AOA perturbation effectively changes the pulsar's assumed position on the sky. This perturbation is of the form

$$\delta t_{\rm bary}(\tau) = \frac{1}{c} (\boldsymbol{r}_E \cdot \hat{\boldsymbol{n}})(1 - D_s/D)[\theta_r(x) - \theta_r(x + b)]_{b=V_\perp \tau} . \tag{3.5}$$

For a pulsar in the ecliptic plane, the dot product reduces to $(AU/c) \cos (\Omega_E t)$ where Ω_E is the orbital frequency of the Earth about the Sun for an assumed circular Earth orbit of one astronomical unit (AU) in radius.

The three plasma propagation terms have different frequency and time-dependences. For an idealized medium where the refraction is produced by discrete lenses whose sizes are much larger than the Fresnel scale, the wavelength dependences are $\delta t_{DM} \propto \lambda^2$, $\delta t_{\rm geo} \propto \lambda^4$, and $\delta t_{\rm bary} \propto \lambda^2$. For media with a broad distribution of length scales, such as is implied by scintillation and angular-broadening measurements, the wavelength dependences are different because diffraction from length scales smaller than the Fresnel scale causes the observed signal to come from a region on the screen of size $D\theta_d \propto \lambda^2$. The exponent of λ is ~ 2 but actually depends on the spectrum of the density fluctuations (eq. [1.1]). The wavelength dependences are discussed further below.

IV. GENERATION OF REFRACTING SCREENS

Two aspects of screen generation are important. First, the *shape* of the power spectrum is of the power-law form of equation (1.1). Second, the *rms phase variation* in the screen must be fixed to match conditions encountered in realistic observing situations.

To generate a phase screen with the correct (average) spectral shape, the Fourier transform of a realization of white noise $W(q)$ is multiplied by a power-law function,

$$S(q) = \begin{cases} q^{-\alpha/2}, & q_O \le q \le q_I ; \\ 0 & \text{otherwise} \end{cases} . \tag{4.1}$$

The low- and high-wavenumber cutoffs are given as q_O and q_I. The Fresnel wavenumber, q_F, and the diffraction wavenumber, q_d, are shown in Figure 1 where $q_F \ll q_d$. The product is inverse Fourier transformed to yield the phase perturbation $\phi(x)$:

$$\phi(x) \overset{\rm FFT}{\Longleftrightarrow} S(q)W(q) . \tag{4.2}$$

An example of one realization of a phase screen for a Kolmogorov spectrum is shown in Figure 2*a* for values of the index $\alpha = 7/3$, 8/3, and 3. We have used a screen amplitude consistent with the *diffractive* scintillations of the millisecond pulsar PSR 1937+21. The phase at 1 GHz wanders over thousands of radians over the 2000 days simulated in this figure. The angular wandering induced by refraction is also shown (Fig. 2*b*). The refraction screen is smoothed by the multipath scale (see eq. [4.6]) to account for the multipath propagation due to diffraction.

The realizations have been calculated so that the length scales on which the rms phase equals unity (which is, by definition, the diffraction scale) is identical for all values of α. It is obvious that the long term fluctuations in both the phase and the refractive angle increase as α gets larger.

To construct screens, we require that the phase amplitude be

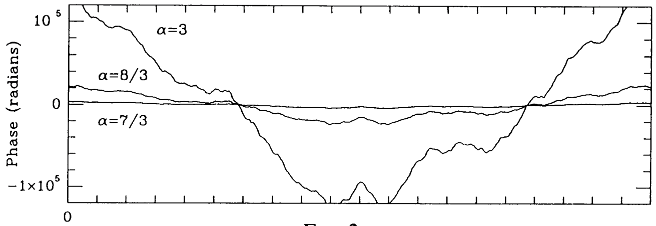

FIG. 2a

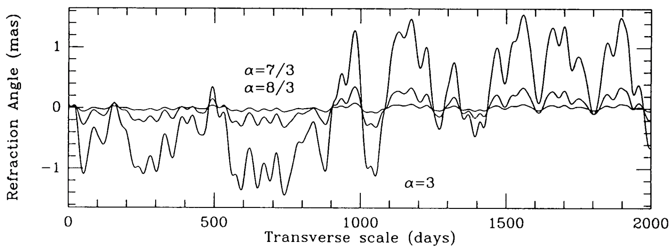

FIG. 2b

FIG. 2.—(a) Examples of phase screens generated by the simulation code for spectrum with index value $\alpha = 7/3$, 8/3, and 3 at a frequency of 1 GHz. The amplitude is the phase perturbations in units of radians and the transverse scale in bin units can be related to a spatial scale by assuming one bin equals the distance traveled in one day at the velocity $V_{\perp}$. (b) The angular wandering of the source position is computed from the refractive bending angle. The refractive angle at 1 GHz is plotted in milliarcseconds for the above phase screens.

consistent with the scintillation bandwidth,[2] a quantity that is measured for most pulsars. The scintillation bandwidth, being a diffractive quantity, is not modeled in our simulation, but it is used as an input parameter to derive the rms amplitude of the phase screen.

A brief review of the scintillation scaling follows. The spatial scale of the intensity scintillation pattern can be related to the scintillation bandwidth $\Delta\nu_d$ and pulsar distance as

$$l_{sp} = \left[\frac{\lambda^2 D \Delta\nu_d}{2\pi c(D/D_s - 1)}\right]^{1/2} . \tag{4.3}$$

This scale is appropriate for a screen at distance D_s from the Earth that is illuminated by spherical electromagnetic waves from the pulsar at distance D. To derive the screen parameters, it is convenient to derive the intensity scale that would be produced if the screen were illuminated by a plane wave:

$$l_d = (1 - D_s/D) l_{sp} . \tag{4.4}$$

The spatial scale of the intensity scintillation pattern defines the size of the scattering disk (FWHM):

$$\theta_d = 2\sqrt{\ln 2}\, \lambda/\pi l_{sp} , \tag{4.5}$$

which, in turn, defines the multipath propagation scale:

$$r_{mp} = \theta_d D_s(1 - D_s/D) , \tag{4.6}$$

that represents the minimum length scale of refractive perturbations that can alter pulse arrival times.

The spatial scale of the diffraction pattern is the $1/e$ length of the intensity covariance function, $\Gamma_I(b)$, which is related to the visibility function $\Gamma(b)$ by

$$\Gamma_I(b) = |\Gamma(b)|^2 , \tag{4.7}$$

where the visibility function is the second moment of the electric field E:

$$\Gamma(b) = \langle E(x)E^*(x + b)\rangle = \exp\left[-\tfrac{1}{2}D_\phi(b)\right] . \tag{4.8}$$

Equation (4.7) holds in the strong scattering regime in which the screen imposes phase perturbations much larger than a radian (e.g., Rickett 1977). The one-dimensional phase structure function is

$$D_\phi(b) = \langle |\phi(x) - \phi(x + b)|^2\rangle , \tag{4.9}$$

where the angular brackets denote ensemble averaging and is proportional to the integrated power density function defined in equation (1.1):

$$D_\phi(b) = 4\pi\lambda^2 r_e^2 \int_0^L dz \int_0^\infty dq[1 - \cos(qb)] P_{\delta n_e}(q) . \tag{4.10}$$

For a one-dimensional screen having a spectrum of the form of equation (1.1), the phase-structure function scales as

$$D_\phi(b) = 2\left(\frac{b}{l_e}\right)^{\alpha - 1} \equiv \left(\frac{b}{l_d}\right)^{\alpha - 1} , \tag{4.11}$$

where l_d is the diffraction scale. At the length scale l_e the visibility function from a plane wave illumination of the screen is $1/e$.[3] We scale the screen amplitude by requiring that the phase-structure function of the simulated screen at a lag of one sample (i.e., $D_\phi[\Delta x]$) be equal to that given by equation (4.11) with $b = \Delta x$.

Measured scintillation bandwidths are usually at frequencies different from those used in our simulation. We therefore scale the measured scintillation bandwidths in a way that is consistent with the slope α used to generate the phase screen. Romani, Narayan, and Blandford (1986) and Cordes, Pidwerbetsky, and Lovelace (1986) give the scaling of scintillation bandwidth with wavelength for two-dimensional screens and three-dimensional media. The analogous scaling laws for one-dimensional screens are

$$\Delta\nu_d \propto \lambda^{-2(\alpha+1)/(\alpha-1)} \tag{4.12}$$

for $1 < \alpha < 3$,

$$\Delta\nu_d \propto \lambda^{-8/(5-\alpha)} \tag{4.13}$$

for $3 < \alpha < 5$, and for $\alpha = 3$,

$$\Delta\nu_d \propto \lambda^{-4} . \tag{4.14}$$

In computing the three interstellar TOA perturbations, we use two refraction screens to mimic two-dimensional AOA variations. The two screens are orthogonal to each other, giving a distinct AOA variation in each direction on the sky. The total geometric delay is computed from the square root of the sum of the squares of the refractive angle from each screen. The dispersion measure induced delay is computed directly from only one of the screens.

The generated refraction screens scale according to the scintillation bandwidth, observing wavelength, power spectrum slope, and pulsar distance. Using the same initial conditions for

[2] The scintillation bandwidth (also called the diffraction and decorrelation bandwidth) is the range of frequencies over which the observed pulsar intensity is correlated. Decorrelation occurs as a result of multipath propagation between the source and the observer. At meter wavelengths, the scintillation bandwidth is commonly in the range of 1–10^4 kHz.

[3] Note that the scale l_e at which the visibility function is $1/e$, the phase structure function is 2 rad^2, while it is half this at the intensity scale l_d.

TABLE 1

PULSAR PARAMETERS USED IN SIMULATION

Pulsar	DM (pc cm^{-3})	Period (ms)	Log $\dot{P}$ (s s^{-1})	D (kpc)	$\Delta\nu_d$ at 1 GHz (MHz)	$V_\perp$ (km s^{-1})
PSR 1620−26........	63	11.075	−18.1[1]	2.1[2]	(0.45)	(200)
PSR 1821−24[3].......	120	3.054	−17.8	5.8[2]	(0.06)	(200)
PSR 1855+09[4].......	13	5.362	−19.8	0.5	4.1[8]	10
PSR 1913+16[5].......	169	59.030	−17.1	5.6	0.01[8]	100
PSR 1937+21[4].......	71	1.558	−19.0	5.0	0.3[9]	50
PSR 1953+29[4].......	105	6.133	−19.5	3.5	(0.1)	(100)
PSR 1957+20[6].......	30	1.607	−19.7[7]	1.0	(4)	(60)

NOTE.—Values in parentheses are assumed. All other values are either measured directly or derived from measurements.

REFERENCES.—(1) McKenna and Lyne 1988; (2) Webbink 1985; (3) Foster *et al.* 1988; (4) Rawley *et al.* 1988; (5) Taylor and Weisberg 1989; (6) Fruchter *et al.* 1988; (7) Fruchter 1988; (8) Dewey *et al.* 1988; (9) Cordes *et al.* 1990.

generating the white noise phase screen allows us to recreate the same phase screen at different wavelengths.

V. FITTING OF PSEUDO–TIMING DATA FOR PSR 1937+21

The millisecond pulsar 1937+21 is the pulsar with the most accurate timing and the greatest rotational stability (Davis *et al.* 1985; Rawley, Taylor, and Davis 1988; Cordes *et al.* 1990). The random measurement errors in the best data obtained to date are ~ 300 ns (Rawley *et al.* 1988). Recent work has shown that arrival times are perturbed by fluctuations that scale predominantly as λ^2 and are most likely variations in dispersion measure (Cordes *et al.* 1990). However, when the λ^2 variations are removed from arrival times, and the data are fitted for pulsar spin parameters, position (on the sky), and proper motion, the residuals still show nonrandom behavior (Taylor 1988). These residuals are due to a process or processes that necessarily scale differently than λ^2. Sources of non-λ^2 processes include (1) higher order refractive delays as discussed in the preceeding sections; (2) intrinsic timing noise in the rotation of the pulsar; (3) errors in the Earth based atomic time standard; (4) errors in the pulsar position introduced by uncertainties in the correction from topocentric to barycentric arrival times; and (5) distortions in the local space-time metric. Processes (2)–(5) are wavelength independent.

In the following section, we study the perturbing effects of the interstellar medium on our ability to extract useful information from arrival time data. We present the simulated data for PSR 1937+21 in detail because, to date, arrival time data from this object provide the best opportunity for measuring parallax and for placing limits on a stochastic gravitational wave background. Data from the other millisecond pulsars will be discussed briefly in the following section. The parameters used for each pulsar are presented in Table 1. Assuming a specific spectrum α for the electron-density distribution and choosing observing frequencies of 0.33, 0.43, 0.75, 1.0, 1.4, and 2.4 GHz, we show the effects of propagation terms on different fits to pulsar arrival time data.

a) Scaling of Individual Terms

Table 2 shows the rms amplitude of the three propagation delays averaged over 20 realizations of a Kolmogorov phase screen $\alpha = 8/3$ for PSR 1937+21 data at six frequencies. In Figure 3 the amplitudes of five terms at 1 GHz that perturb the simple polynomial spin-down of the pulsar are separated and displayed on individual panels. The six month parallax term, the annual term from proper motion, and the three propagation terms due to the barycentric, geometrical, and dispersion delays are plotted.

Our ability to fit for the astrometric terms of proper motion and parallax are strongly affected by the assumed slope of the electron density power spectrum and the distance to the pulsar. The amplitude of the parallax term (see eq. [2.1]) is

$$t_{\text{par}} = \frac{1}{2}\frac{r_E^2}{cD}\left[1 - (\hat{\boldsymbol{r}}_E \cdot \hat{\boldsymbol{n}})^2\right] , \tag{5.1}$$

so the zero to peak amplitude is

$$\max\,(t_{\text{par}}) \simeq 1.2(\mu\text{s}) D_{\text{kpc}}^{-1} \cos^2\,(\lambda_e) , \tag{5.2}$$

where λ_e is the ecliptic latitude. When we place the pulsar 1937+21 at a distance of 1 kpc (rather than the established distance of 5 kpc, Heiles *et al.* 1983), we are able to solve for the parallactic distance using four frequency data collected between 0.33 and 1.0 GHz. Our solution even solves for the index of refractive perturbations, although this is not a very reliable solution (see Table 5A) and discussion below.

TABLE 2

AMPLITUDES OF PROPAGATION TERMS AT SIX FREQUENCIES FOR PSR 1937+21

Term	333 (MHz)	430 (MHz)	750 (MHz)	1 (GHz)	1.4 (GHz)	2.38 (GHz)
Geometric delay (μs)	1.1	0.7	0.2	0.1	<0.1	$\ll 0.1$
Barycentric error (μs)	1.6	1.2	0.5	0.3	0.2	0.1
Dispersion delay (μs)	14.5	8.7	2.9	1.5	0.8	0.3

NOTE.—Amplitude of each individual delay term for PSR 1937+21 is given as the root mean square of the term in μs. The values were derived from 20 independent realizations of a four year simulation using phase screens generated from a Kolmogorov power spectrum ($\alpha = 8/3$). The refractive screens were smoothed by the multipath scale.

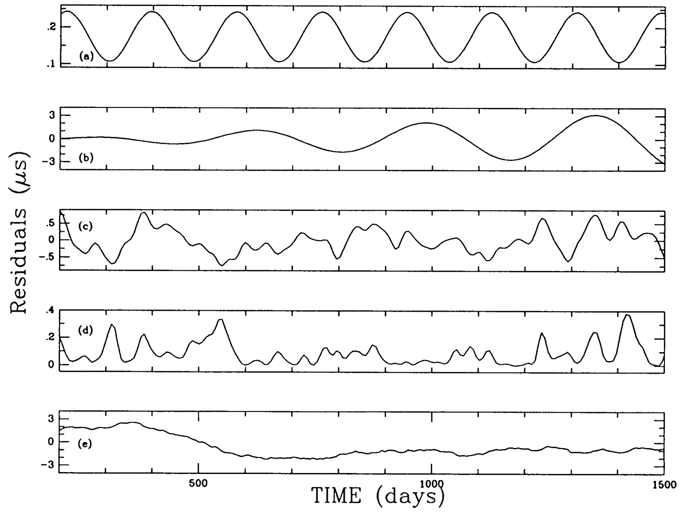

FIG. 3.—The five panels each represent a single term added to the arrival time perturbation. Collectively these terms produce the errors generated by the phase and refraction screens. The panel show (*a*) parallax, (*b*) proper motion, (*c*) the barycentric correction error induced by angular wandering of the source position, (*d*) the amplitude of the geometric delay, and (*e*) the dispersion measure delay. All terms were generated using a Kolmogorov power spectrum at a frequency of 1 GHz and cover a four year time period.

The dominant effect on the residuals is the variable dispersion measure delay (Fig. 3), which produces peak-to-peak arrival time errors as large as $\sim 6\ \mu s$ at 1 GHz over four years. Since dispersion measure delays scale strictly as λ^2, dual frequency observations can be used to remove them. Unfortunately, this may be insufficient, since, at the same observing frequency, both the barycentric and geometric propagation delays contribute peak-to-peak errors of $\sim 1.5\ \mu s$ and $\sim 0.4\ \mu s$ respectively (see Fig. 3). At higher frequencies the propagation effects will be reduced. Table 3 shows the scaling of the arrival time residuals from each perturbation term at 1 GHz over 2, 4, and 8 year time intervals. Both the geometrical delay and the barycentric delay saturate with time scales of a few months as expected from the multi-path propagation scale. The dispersion measure term grows proportionally to $\tau^{5/6}$ until the outer scale, $l_O = 2\pi/q_O$, is reached (≥ 1000 years). The scalings of the three propagation delay terms with frequency depend on the index of the electron density power spectrum. Table 4 shows the propagation delay terms for different values of the electron-density power spectrum α.

b) *Multiple Frequency Data*

One of the goals of our simulation is to investigate the feasibility of removing λ dependent effects. We generate arrival times, according to equation (2.1), perturbed by the phase screen with a spectral index $\alpha = 8/3$, using a model for the pulsar 1937+21 as given in Table 1 except that a distance of 1 kpc is assumed. We then fitted the simulated arrival time data for the spin-down and astrometric parameters involving P, $\dot{P}$, $\hat{\boldsymbol{n}}$, $\boldsymbol{\mu}$, and distance D. An initial fit for the pulsar spin polynomials is made to the TOA's at each frequency. We call these residuals $\hat{R}_0(t, \lambda)$. The multifrequency residuals are then fitted at fixed times t for a wavelength-dependent function of the form

$$\hat{R}_0(t, \lambda) = a_t \lambda^2 + b_t \lambda^\gamma + c_t\ , \qquad (5.3)$$

where the coefficient a_t is the amplitude of the dispersion delay introduced by the changing electron-column density, b_t is the amplitude of the dominant nondispersive delays with a wavelength dependence that scales with the spectrum of the perturbing screen, and c_t is a constant term that includes wavelength independent rotational variations. The spectral index of the dominant refraction effects is γ. We assume that only one of the barycentric or geometric terms dominate the data in our simulation. The parameters a_t, b_t, and c_t are determined uniquely at each epoch, while γ is solved globally so that the general solution minimizes the rms residuals. The resulting parameters are used to remove the frequency dependent perturbations according to:

$$\delta R_t = \hat{R}_0(t, \lambda) - a_t \lambda^2 - b_t \lambda^\gamma = c_t\ . \qquad (5.4)$$

The corrected wavelength independent residuals δR_t are used to fit for new spin-down terms, proper motion, and parallax terms.

TABLE 3

AMPLITUDE OF PROPAGATION TERMS AT 1 GHz SCALED WITH TIME ($\alpha = 8/3$)

Time	Geometric delay (μs)	Barycentric error (μs)	Disperson delay (μs)
$T = 2$ yr.....	0.068	0.33	1.10
$T = 4$ yr.....	0.076	0.34	1.55
$T = 8$ yr.....	0.081	0.35	1.96

NOTE.—The amplitude of each delay term is given in microseconds. The values given are the root mean squares of each term computed by the simulation over the given time period. Twenty phase screens were generated using a Kolmogorov power spectrum ($\alpha = 8/3$). The refractive screens where smoothed by the multipath scale. The terms simulate arrival time data from PSR 1931+21.

TABLE 4

AMPLITUDE OF PROPAGATION TERMS AT 1 GHz SCALED WITH α

Index (α)	Geometric delay (μs)	Barycentric error (μs)	Dispersion delay (μs)
2.33.......	$\ll 0.1$	0.1	0.2
2.67.......	0.1	0.3	1.5
3.00.......	1.6	1.6	9.1

NOTE.—The amplitude of each delay term is in microseconds. The values given are the root mean squares of each term computed by the simulation over the given time period. Twenty refractive screens where smoothed by the multipath scale. The simulation covered a four year time period. The terms simulate arrival time data from PSR 1937+21.

c) *The Fit*

We fitted the multifrequency timing data in three different manners. First, we fit for only spin-down and astrometric parameters (effectively setting $a_t = b_t = 0$ in eq. [5.1]). Second, we fit only for DM variations, fixing $b_t = 0$. Finally, we fit the data using all the terms in equation (5.1). The results of the three different fitting procedures are given in Table 5A. The simulated data were fitted across four frequencies: 0.33, 0.43, 0.75, and 1.0 GHz. Figure 4 displays the DM perturbation and the fitted dispersion measure sampled once every two weeks over four years. The agreement between the dispersion measures generated by the phase screen and the fit dispersion after running the simulation demonstrates the necessity of removing dispersion measure variations from the timing data in order to obtain microsecond timing precision. Angle-of-arrival variations from the barycentric delay term are the dominant source of the differences. Since this term scales very closely to λ^2, the fitted DM removes more λ^2 power than expected from δt_{DM} alone.

TABLE 5

A. FITTED DATA FROM PSR 1937+21 1000 MHz MAXIMUM FREQUENCY[a]

Term	Value	Initial Fit at 1 GHz	λ^2 Fit	λ^2 and λ^γ Fit
f(Hz)	641.85	$\pm 5.2 \times 10^{-12}$	$\pm 5.4 \times 10^{-12}$	$\pm 4.4 \times 10^{-12}$
$\dot{f}$(Hz s^{-1})	1.08×10^{-18}	$\pm 8.5 \times 10^{-20}$	$\pm 8.9 \times 10^{-20}$	$\pm 7.2 \times 10^{-20}$
μ_α(mas)	-0.259	-0.400 ± 0.022	-0.285 ± 0.023	-0.260 ± 0.018
μ_δ(mas)	-0.436	-0.434 ± 0.027	-0.401 ± 0.029	-0.426 ± 0.023
D (kpc)	1.0	1.4 ± 3.4	2.6 ± 2.0	2.0 ± 1.0
$\sigma_{rms}(\mu s)$	0.1	0.7	0.7	0.6
index γ	1.63[b]			4.7 ± 0.8

NOTE.—The data used in this table came from one realization of simulated timing data from PSR 1937+21. The values were derived from a four year simulation using a phase screen generated from a Kolmogorov power spectrum ($\alpha = 8/3$). The data were fit over four frequencies: 333, 430, 750, and 1000 MHz.

[a] Spectral index $\alpha = 8/3$.

[b] Assuming angle-of-arrival variations from the barycentric correction term dominate geometric delays.

B. FITTED DATA FROM PSR 1937+21 2380 MHz MAXIMUM FREQUENCY[a]

Term	Value	Initial Fit at 1 GHz	λ^2 Fit	λ^2 and λ^γ Fit
f(Hz)	641.85	$\pm 5.2 \times 10^{-12}$	$\pm 3.6 \times 10^{-12}$	$\pm 2.5 \times 10^{-12}$
$\dot{f}$(Hz s^{-1})	1.08×10^{-18}	$\pm 8.5 \times 10^{-20}$	$\pm 5.9 \times 10^{-20}$	$\pm 4.1 \times 10^{-20}$
μ_α(mas)	-0.259	-4.00 ± 0.022	-0.279 ± 0.015	-0.266 ± 0.010
μ_δ(mas)	-0.436	-0.434 ± 0.027	-0.415 ± 0.019	-0.431 ± 0.013
D(kpc)	1.0	1.4 ± 3.4	1.7 ± 0.6	1.4 ± 0.3
$\sigma_{rms}(\mu s)$	0.1	0.7	0.5	0.3
index γ	1.63[b]			5.4 ± 0.8

NOTE.—The data used in this table came from one realization of simulated timing data from PSR 1937+21. The values were derived from a four year simulation using a phase screen generated from a Kolmogorov power spectrum ($\alpha = 8/3$). The data were fit over five frequencies: 333, 430, 750, 1000 and 2380 MHz.

[a] Spectral index $\alpha = 8/3$.

[b] Assuming angle-of-arrival variations from the barycentric correction term dominate geometric delays.

C. FITTED DATA FROM PSR 1937 + 21 5000 MHz MAXIMUM FREQUENCY[a]

Term	Value	Initial Fit at 1 GHz	λ^2 Fit	λ^2 and λ^γ Fit
f(Hz)	641.85	$\pm 5.2 \times 10^{-12}$	$\pm 1.2 \times 10^{-12}$	$\pm 9.0 \times 10^{-13}$
$\dot{f}$(Hz s^{-1})	1.08×10^{-18}	$\pm 8.5 \times 10^{-20}$	$\pm 1.9 \times 10^{-20}$	$\pm 1.5 \times 10^{-20}$
μ_α(mas)	-0.259	-0.400 ± 0.022	-0.267 ± 0.005	-0.265 ± 0.004
μ_δ(mas)	-0.436	-0.434 ± 0.027	-0.438 ± 0.006	-0.438 ± 0.005
D(kpc)	1.0	1.4 ± 3.4	1.05 ± 0.07	1.08 ± 0.06
$\sigma_{rms}(\mu s)$	0.1	0.69	0.15	0.12
index γ	1.63[b]			3.8 ± 0.6

NOTE.—The data used in this table came from one realization of simulated timing data from PSR 1937+21. The values were derived from a four year simulation using a phase screen generated from a Kolmogorov power spectrum ($\alpha = 8/3$). The data were fit over four frequencies: 1000, 1400, 2380, and 5000 MHz.

[a] Spectral index $\alpha = 8/3$.

[b] Assuming angle-of-arrival variations from the barycentric correction term dominate geometric delays.

Figure 5*a*–*b* displays the residuals for four frequencies of data corrected for a simple λ^2 term and after correcting for a λ^2 plus λ^γ terms to remove the dispersion measure and refractive delays. The final residuals after fitting for the λ^2 term are ~ 0.7 μs, while after fitting for the λ^2 and λ^γ term they are reduced to a level of ~ 0.6 μs rms, where $\gamma = 4.7 \pm 0.8$. The ~ 0.6 μs residuals represent the limit obtainable by removing a dispersive term proportional to λ^2 plus fitting for a refractive term proportional to λ^γ in the 0.33 GHz to 1.0 GHz frequency interval.

Adding an additional frequency at 2.4 GHz (Table 5B) lowers the final residuals to 0.5 μs for a simple λ^2 fit and to 0.3 μs for a λ^2 plus λ^γ fit. The solved exponent term was $\gamma = 5.4 \pm 0.8$. The fitted values for the proper motion and parallax are better than the values obtained using only the lower frequency data. While fitting for the extra term λ^γ does improve the fit when the 2.4 GHz data are included, it does so only marginally for the four frequencies between 0.33 and 1.0 GHz.

Table 5C gives the results from a four frequency fit in the interval between 1.0 and 5.0 GHz. The results show that all of the pulsar spin and astrometric terms are solved for with a simple λ^2 to account for the dispersion measure variations. Adding an additional term proportional to λ^γ as we did above does not improve the solutions. Above 1 GHz the refractive delays have become sufficiently small that they are negligible in

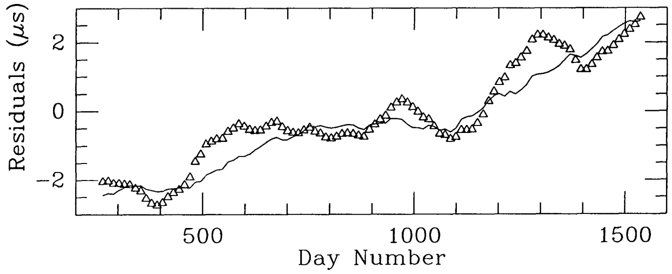

FIG. 4.—The ability of dual frequency measurements to remove the dispersion delay is demonstrated. The solid line represents the original phase screen generated by the simulation. The triangle represent the best estimate of the dispersion delay at each epoch computed from dual-frequency data between 430 MHz and 1 GHz. The post-fit residuals are displayed for a simulated frequency of 1 GHz.

our simulated data. Adding the extra term only decreases the number of degrees of freedom and improves the residuals accordingly. Strong coupling between terms does not allow easy separation and recovery of the true terms. The number of degrees of freedom decreases from roughly 300 when fitting for a λ^2 term to less than 200 when the λ^γ term is added. Therefore, the nearly factor of 2 improvement in the residuals is better than expected from a 33% increase in the number of parameters, when the high-frequency data are added.

The four-frequency fits tend to minimize the residuals and solve for refractive indexes giving values of γ between 4 and 5. This is much larger, and implies a much steeper turbulence spectrum, than expected from the input model where we know the refractive perturbations are dominated by AOA variations. The expected index γ from AOA variations produced by a Kolmogorov spectrum is 1.63 (49/30). The reason for this discrepancy in the simulated data is that the refractive perturbations have a "beam" size set by the multipath propagation scale that depends directly on the wavelength of observation. For PSR 1937+21 the multi-path scale at 1.0 GHz is 2.6×10^{13} cm and at 0.43 GHz the multi-path scale grows to 1.7×10^{14} cm, while the amplitude of the geometrical delay term decreases from 0.7 μs at 0.43 GHz to 0.1 μs at 1.0 GHz. The angle-of-arrival term displays more rapid variations at shorter wavelengths than at longer wavelengths, thus making the fitting process for a λ^γ term intrinsically difficult. The χ^2 minimization process used to solve for the refractive index γ returns asymmetric errors with a much steeper gradient toward small values of the index and a shallow gradient toward large values. Thus any uncertainty in the value γ will tend to be biased toward larger values and hence a steeper spectrum.

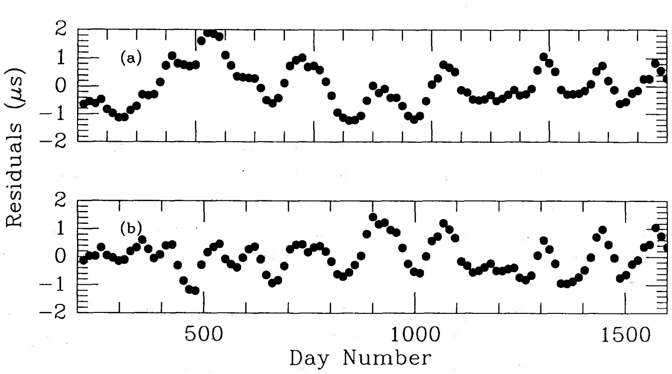

FIG. 5.—(*a*) The final residuals are plotted for four frequency data (333, 430, 750, MHz, and 1 GHz) fit for spin and astrometric parameters plus dispersion measure; and (*b*) the same as in (*a*) plus fitting for refraction induced perturbations ($\propto \lambda^\gamma$). The final residuals have an rms amplitude of 0.7 μs and 0.6 μs, respectively. The same data are tabulated in Table 5A.

d) *Non-Kolmogorov Spectra*

Refraction effects are a strong function of the spectral index of the electron-density turbulent spectrum. Increasing the slope from the Kolmogorov value of $\alpha = 8/3$ to $\alpha = 3$ substantially increases the amplitudes of the dispersion measure and geometric delay terms.[4] At 1 GHz the rms amplitude of these terms averaged over 20 realizations is 1.6 μs for the geometric delay and barycentric correction terms and 9.1 μs for the dispersion delay (see Table 4). After applying a four wavelength fit over the interval 0.33 to 1.0 GHz we conclude that the use of a λ^2 term is insufficient to recover properly the original perturbing phase screen and to fit for proper motion. Adding the λ^γ term did not substantially improve the fits. The refractive power still left in the corrected residuals exceeds the amplitude of the astrometric terms of proper motion and parallax.

Decreasing the slope of the power spectrum to $\alpha = 7/3$ lowered the rms amplitude of the geometric delay at 1 GHz to 0.1 μs and the dispersion measure to 0.2 μs over a single four year simulation. Fitting for dispersion measure removed almost all of the variations due to the changing electron column density. The addition of a λ^γ term to the fitting did not improve the pulsar parameter estimation and reduced the distance estimate errors only by a marginal amount. Fitting for the refractive term was not very significant in this case, due to its negligible amplitude at this power spectrum slope (see Table 4).

e) *Big vs. Small Telescopes*

In order to optimize a millisecond pulsar observing program we studied the possibility of measuring parallax from pulsar 1937+21 using a small telescope. To make a comparison, we assume that both telescopes have the same integration time (per arrival time) and bandwidth. We also assume that the number of arrival times (epochs) for the smaller telescope is the square of the ratio $(G/T_{sys})_{big}/(G/T_{sys})_{small}$ times the number of arrival times for the larger telescope, where G is the telescope gain and T_{sys} is the system temperature. Doubling the ratio of G/T_{sys} in one telescope requires that the number of samples obtained with the other instrument must be quadrupled to keep the net radiometer error the same.

As a specific case, we assume a large antenna with G/T_{sys} four times larger than for a small antenna. Simulated arrival time data were generated for PSR 1937+21, with observation epochs every 16 days for 1200 days, at a distance of 1 kpc and an electron-density power spectrum index $\alpha = 8/3$. A white-noise background (0.1 μs) was added to the arrival time errors. A second data set was generated with daily sampling over the same 1200 days, but the white noise background was four times higher.

Simulated data from four frequencies (0.33, 0.43, 1.0, and 1.4 GHz) were able to reproduce the original pulsar parameters, including a solution for the parallactic distance, after removing λ^2 and λ^γ terms. The formal uncertainties in the individual astrometric and screen index parameters are smaller in the case of the smaller telescope with frequent sampling. The more frequent sampling obtained with the smaller telescope was better

[4] The spectrum is always normalized at the diffraction wavenumber so that a steeper index implies larger refraction effects for a fixed diffraction effect.

TABLE 6

PARALLAX FITTING OF BIG VS. LITTLE TELESCOPE

TERM	VALUE	BIG TELESCOPE Initial	BIG TELESCOPE λ^2	BIG TELESCOPE λ^2 and λ^γ	LITTLE TELESCOPE Initial	LITTLE TELESCOPE λ^2	LITTLE TELESCOPE λ^2 and λ^γ
f(Hz)	641.85	$\pm 2.8 \times 10^{-11}$	$\pm 3.6 \times 10^{-12}$	$\pm 3.5 \times 10^{-12}$	$\pm 3.3 \times 10^{-12}$	$\pm 1.2 \times 10^{-12}$	$\pm 1.3 \times 10^{-12}$
$\dot{f}$(Hz s^{-1})	1.08×10^{-18}	$\pm 3.8 \times 10^{-19}$	$\pm 6.8 \times 10^{-20}$	$\pm 6.7 \times 10^{-20}$	$\pm 6.2 \times 10^{-20}$	$\pm 2.3 \times 10^{-20}$	$\pm 2.4 \times 10^{-20}$
μ_α(mas)	−0.259	-0.315 ± 0.083	-0.234 ± 0.015	-0.224 ± 0.015	-0.221 ± 0.014	-0.241 ± 0.005	-0.227 ± 0.005
μ_δ(mas)	−0.436	-0.292 ± 0.105	-0.501 ± 0.019	-0.546 ± 0.019	-0.362 ± 0.017	-0.485 ± 0.006	-0.537 ± 0.007
D(kpc)	1.0	...	...	4.2 ± 2.9	...	...	3.0 ± 0.6
$\sigma_{\rm rms}(\mu$s)	...	0.9	0.3	0.3	0.9	0.5	0.5
γ		...	...	3.7 ± 0.5	...	...	3.2 ± 0.3
observations		75			1200		
$\sigma(\mu$s) white noise		0.1			0.4		
T(days)		1200			1200		

at determining the wavelength scaling of the refractive delay term. Table 6 shows the quality of the fit to the pulsar parameters for frequently sampled observations on a small telescope versus sparse sampling on a larger telescope. We find that it is better to make daily observations with a small telescope than less frequent observations using a large telescope.

f) *The Dominant Source of Uncertainty*

The dominant refraction term responsible for the uncertainty in our fits is the barycentric correction term for power spectra with slopes equal to 8/3. The peak-to-peak wandering of the source position can be as large as ~ 1 mas corresponding to an arrival time delay of ~ 1.2 μs at 1 GHz at a distance of 1 kpc. Because the amplitude of this term scales as $\lambda^{1.63}$ for a Kolmogorov spectrum, a large fraction of this term is absorbed into the dispersion measure fit (see Fig. 4). The unabsorbed part of the term will be nearly frequency independent. Figure 6 shows the high degree of correlation between residuals from the fit for dispersion measure only with the barycentric error term used in the simulation. Figure 7 gives the crosscorrelation function between these two time series at all possible lags. The peak correlation has a value of 0.7 at zero lag, where 1.0 at zero lag would be perfect correlation. If refractive effects contribute to the uncerainty of the timing data in PSR 1937+21, the simulation suggests that the dominant term is the wandering of the source position from AOA variations.

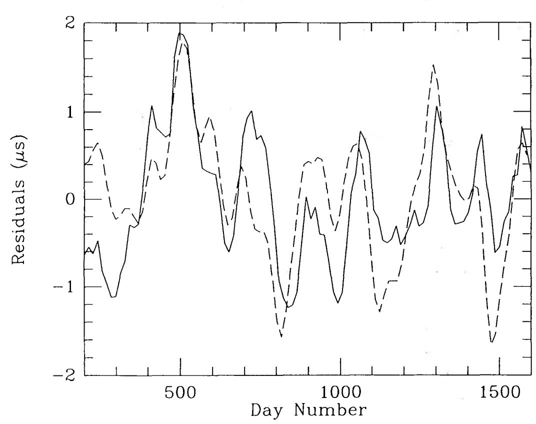

FIG. 6.—The solid line represents the barycentric correction error from uncertainty in the true pulsar position as added to the simulated arrival times before solving for the pulsar spin and astrometric parameters. The dashed line traces the frequency corrected final residuals after fitting for the pulsar's spin, astrometric, and dispersion measure parameters. The two terms show a high degree of correlation.

VI. OTHER PULSARS

As with PSR 1937+21, we simulated TOA's for other pulsars using the data given in Table 1 to scale their scattering screens. Data were generated at three radio frequencies: 430 MHz, 750 MHz, and 1.0 GHz for each pulsar in the list. The amplitudes of various propagation delay terms for each of these pulsars as estimated by our simulations are given in Table 7. A simple dispersion measure fit was applied through the three frequency arrival times. The parameters were compared with the original parameters and are given in Table 8. The final residuals from each pulsar were between three and eight times the input 0.1 μs white noise level. Refraction induced AOA variations contribute the excess power.

In all cases, the proper motion is easily solved for while the distance is estimated to within 25% of the "true" value for only three objects (PSR's 1620−26, 1855+09, and 1957+20). Fitting data from three frequencies for a λ^2 term does a respectable job of removing the dispersion measure variations and bringing the simulated timing residuals below a microsecond in rms fluctuations. One microsecond timing resolution may not be currently within observational possibilities for some of the objects included in this analysis. Low-flux densities require long integration times, wide bandwidths, and large collecting areas. These observational constraints are limited by the finite amount of time available on large telescopes and the limited bandwidth capability of current pulsar timing hardware.

The above analysis was predicated on several assumptions

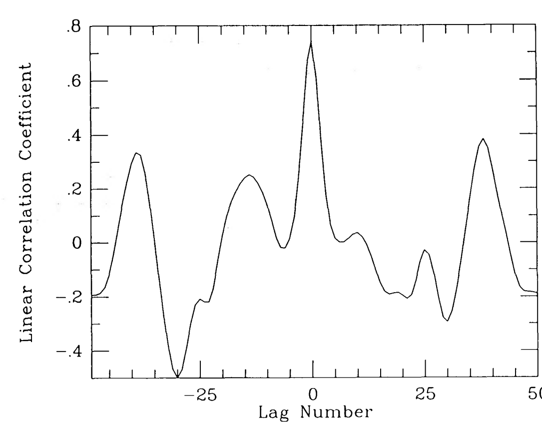

FIG. 7.—The linear correlation coefficient computed between the two terms shown in Fig. 6 is plotted as a function of separation lag. The highest point of correlation gives a value of 0.7 at lag zero.

TABLE 7

AMPLITUDES OF PROPAGATION TERMS AT 1 GHz

Pulsar	Geometric delay (μs)	Barycentric error (μs)	Dispersion delay (μs)
PSR 1620−26.......	0.08	0.42	4.2
PSR 1821−24.......	0.24	0.47	6.4
PSR 1855+09.......	<0.01	0.26	0.03
PSR 1913+16.......	0.37	0.78	7.4
PSR 1953+29.......	0.15	0.57	3.5
PSR 1957+20.......	0.02	0.36	0.7

NOTE.—The amplitude of each delay term is given in microseconds. The values given are the root mean squares of each term computed by the simulation over a four year time period. The phase screen was generated using a Kolmogorov power spectrum ($\alpha = 8/3$). The refractive screens were each smoothed by the multipath scale. These data represent a single realization of a phase screen.

that are in fact probably not appropriate to all fast pulsars. We have assumed that the background noise is truly Gaussian in nature and therefore additive. (See Cordes, Foster and Backer 1990 for a discussion of timing errors that are independent of propagation effects.) We have kept the noise level deliberately low, $\simeq 0.1$ μs, to allow us to "see" the geometric delay at high frequencies. This level of background noise is probably only appropriate for the fastest and brightest millisecond pulsars. The peak flux density at 1.4 GHz for 1937+21 is $\sim$200 mJy (Erickson and Mahoney 1985), a factor of nearly 10 brighter than all the other fast pulsars studied by this simulation. On a purely signal-to-noise basis we would expect the residuals to be an order of magnitude larger for these other pulsars. Hence, determination of the parallax distance will be correspondingly more difficult. The lower flux density also makes the AOA and other refraction induced perturbations less important.

The three objects that show the most potential for measuring parallactic distances are PSR 1620−26, PSR 1855+09, and PSR 1957+20. Pulsar 1620−26 is located in the globular cluster M4 at a distance of 2.1 kpc (Webbink 1985). While this parallax measurement would be interesting as a check on the globular cluster distance estimate, it also will prove to be more difficult than the other two. The pulsar has a rotational period of 11.08 ms and a peak flux density at 1.4 GHz of $\sim$30 mJy (Foster, Fairhead, and Backer 1990). Microsecond level timing will require a timing accuracy better than 0.1 milliperiod. This object is located outside of the Arecibo declination range and will require longer integration times to obtain comparable sensitivity.

Pulsar 1855+09 appears to be a better candidate for measuring parallax. It has the smallest dispersion measure of all known millisecond pulsars and is estimated to be at a distance of only 0.5 kpc. Our simulations easily solve for the parallax term to within 6% of the "true" value. The pulsar is observable between 0.45 and 3.0 GHz (Foster, Fairhead, and Backer 1990) due to its "flat" flux density spectrum, thus refractive perturbations can be minimized by observing at the highest possible frequencies.

The other nearby millisecond pulsar, 1957+20, should also provide a system for measuring parallax. We estimate that a solution with 20% accuracy is obtained after four years of observations between 0.43 and 1.0 GHz. The fact that the system is in an 8 hr binary orbit and regularly eclipsed by its companion (Fruchter, Stinebring, and Taylor 1988) will increase the difficulty of making this measurement. The presence of ionized gas surrounding the companion increases the dispersion measure delay by 0.017 pc cm^{-3} following the eclipse. There may also be an additional ionized region surrounding the entire system increasing the amplitude of dispersion measure and refractive variations at orbital phases far from the eclipse region. These perturbations will contribute to the formal timing uncertainty and perhaps limit the ultimate timing precision.

VII. STRUCTURE FUNCTION ANALYSIS

Our simulations show that data taken at several frequencies can be fitted to remove most of the arrival time perturbations but that it is difficult to infer the slope of the wavenumber spectrum by fitting for the wavelength dependence of the nondispersive TOA fluctuations. Consequently we have used our simulations to explore alternative means for estimating the spectrum.

The phase-structure function (eq. [4.11]) gives complementary information about the wavenumber spectrum because it

TABLE 8

SIMULATED PARALLAX AND PROPER-MOTION FITS FOR MILLISECOND PULSARS

Pulsar	$\sigma_{\rm rms}(\mu s)$[a]	D(Kpc)	μ_α(mas)	μ_δ(mas)
PSR 1620−26.......	0.47	1.9 ± 0.4	-1.04 ± 0.03	-1.27 ± 0.15
PSR 1821−24.......	0.31	3.0 ± 0.7	-0.97 ± 0.02	-1.37 ± 0.44
PSR 1855+09.......	0.35	0.52 ± 0.03	-0.99 ± 0.01	-1.03 ± 0.02
PSR 1913+16.......	0.78	13.6 ± 54.6	-1.03 ± 0.02	-0.91 ± 0.03
PSR 1953+29.......	0.57	-2.5 ± 2.0	-1.03 ± 0.02	-1.04 ± 0.02
PSR 1957+20.......	0.34	1.1 ± 0.2	-1.01 ± 0.01	-1.01 ± 0.01

NOTE.—The frequencies 333, 430, 750, and 1000 MHz were used for the four frequency fit. All simulations assume a proper motion of $\mu_\alpha = -1.0$ mas and $\mu_\delta = -1.0$ mas.

[a] $\sigma_{\rm rms}$ the postfit residuals level after removing a λ^2 term (includes 0.1 μs of a white-noise background).

scales in a manner sensitive to the wavenumber spectral index α. It is possible to estimate the phase-structure function from dispersion measure perturbations, $\delta t_{DM}(\tau)$, that measure the difference in TOA perturbation between two epochs separated by time τ (eq. [3.2]):

$$D_\phi(b) = (2\pi\nu)^2 \langle [\delta t_{DM}(\tau)]^2 \rangle_{\tau=b/V_\perp} . \quad (7.1)$$

In writing equation (7.1) we assume that the effective transverse speed $V_\perp$ convects a frozen phase screen across the line of sight.

We have estimated $D_\phi(b)$ for phase screens at 1 GHz by using equation (7.1) and the δt_{DM} perturbation produced by the screen using the simulated PSR 1937+21 data.[5] The results are shown in Figure 8 (with τ as the independent variable) for irregularity spectra with $\alpha = 7/3$, 8/3, and 3. In addition to the estimated structure function, we show the diffraction time scale $\tau_d \equiv l_e/V_\perp$ that, by definition, gives $D_\phi(V_\perp r_d) = 1$. The lines in Figure 8 with slopes of $\alpha - 1 = 4/3$, 5/3, and 2 are the theoretical structure functions (The scaling $D_\phi \propto \tau^{\alpha-1}$ holds for a one-dimensional screen; the exponent is $\alpha - 2$ for two-dimensional screens.) Over a five decade range in τ, the theoretical lines and the computed structure functions estimated from one realization of pseudodata agree. For large lags, b, the estimated and theoretical structure functions disagree because these lags are comparable to the lengths of the data spans. The structure functions at large lags are clearly larger for increasing α. This is to be expected because larger values of α imply more power in the large irregularities that cause dispersion measure variations.

Figure 9 shows the phase-structure functions estimated from the *total* arrival time perturbation produced by the screen. Of course, equation (7.1) does not hold for the total arrival time perturbation, but in the limit where DM variations *dominate* the perturbation, equation (7.1) may be used as an approximation. Figure 9 demonstrates that the variance in TOA perturbations is in excess of that produced solely by DM variations, particularly at lags below 100 days. The logarithmic slopes of the structure functions in this lag range are smaller than the theoretical slopes by a few tenths.

[5] Note that with simulated data, we can isolate this term, but with real data this is not possible unless the barycentric and geometric terms are negligible.

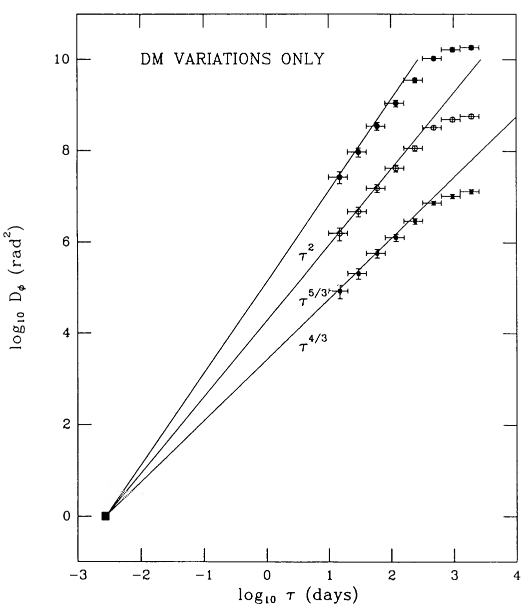

FIG. 8.—The phase structure function for dispersion measure variations generated by the simulation code for different index of the power spectrum are plotted. The closed circles assumed a power spectrum slope of $\alpha = 3$, the open circles assumed $\alpha = 8/3$, and the closed squares assumed $\alpha = 7/3$. The expected slopes scaled from the diffraction bandwidth are drawn on the same figure.

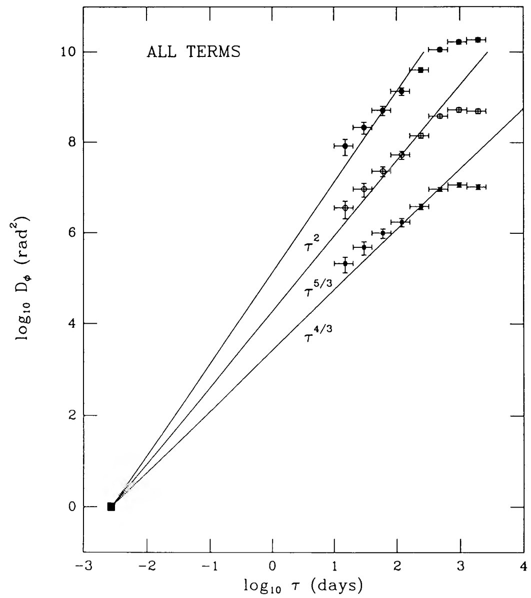

FIG. 9.—The same phase structure function is plotted as in Fig. 8, but this time the refractive terms in the arrival time data are included. Note the excess power at all lags below 100 days from the refraction terms.

The simulation results can be compared with structure functions estimated by Cordes *et al.* (1990; see also Rickett 1988) for the millisecond pulsar 1937+21. Dual-frequency data were used to estimate $DM(t)$ under the assumption that AOA variations were negligible. The time series $DM(t)$ was then used to calculate the structure function of the phase. The real data yield structure function values (Fig. 13 of Cordes *et al.* 1990) that fall between theoretical lines $D_\phi \propto \tau^{5/3}$ and τ^2. Moreover, the logarithmic slope for lags $\tau \approx 30$ to 300 days is much flatter than any of the simulated data. Some flattening may be due to AOA effects, but most of it is probably due to contamination by other effects, as discussed by Cordes *et al.* (1990).

To summarize, the simulation results indicate that, in principle, the structure function can be used to constrain α but that, in practice, it is difficult to use the structure function to determine α to better than about one-third.

VIII. DETECTABILITY OF REFRACTION EVENTS FROM INDIVIDUAL PLASMA CLOUDS

Fiedler *et al.* (1987) reported several deterministic events in the radio "light curves" of active galactic nuclei from a monitoring program conducted with the Green Bank interferometer. The inferred sources of these events are AU sized plasma clouds with a space density of 10^2 per cubic parsec. The largest "event" gives a size of 7 AU and an electron-density enhancement of 4×10^3 cm^{-3}. Two additional, but smaller amplitude events were also reported. A dispersion measure change of ~ 0.13 pc cm^{-3} along the line of sight to a pulsar would be produced by such a cloud.

High-precision timing of pulsars can place constraints on the amplitude and frequency of deterministic events in the interstellar medium. If a cloud passed in front of the pulsar 1937+21, it would perturb the arrival time residuals. The duration and signature of a deterministic event depends on the observing frequency. Multifrequency monitoring of millisecond pulsars should place a limit on the amplitude and frequency of refractive effects in the interstellar medium.

The size and density distributions of these deterministic plasma clouds are unknown. From the Fiedler *et al.* data we expect a single plasma cloud (of a large enough size to produce $\Delta DM = 0.1$) to cross any line-of-sight roughly once every hundred years. Assuming that the clouds have a logarithmic size distribution of slope -1, we might expect clouds that produce $\Delta DM = 0.001$ to cross a line of sight at a rate of about once per year. A $\Delta DM = 0.001$ is the amplitude of variations seen in the dispersion measure variations from PSR 1937+21 over one year time scales (Cordes *et al.* 1990), but these are completely consistent with those expected from a Kolmogorov spectrum. A perturbation producing a $\Delta DM = 0.01$ might occur once every 10 years.

The signature of a small event on pulsar arrival time residuals is shown in Figure 10. The data simulate an event from PSR 1937+21 at 1 GHz. The mean DM perturbation is 8×10^{-3} pc cm^{-3}, slightly less than 1/15 the size estimated by Fiedler *et al.* In terms of the underlying phase screen the amplitude of the event rises eight times above the rms of the phase screen. The underlying phase screen obeys a Kolmogorov power distribution. Note the characteristic double-peaked caustic structure in the timing residuals shown in Figure 10. The residuals around the caustic are all positive valued indicating they are delayed from their mean value. An even larger refractive event could cause the phase delay of the pulse to wrap by more than one period. More than seven years of data have been collected from PSR 1937+21 since its discovery in 1982. No such event has been seen in the published data. Final residuals of 1 μs at 1 GHz place a limit on the electron-column density fluctuations due to discrete structures to be less than 2.4×10^{-4} pc cm^{-3} in DM units.

IX. SUMMARY AND CONCLUSIONS

We have simulated interstellar propagation effects on the arrival time precision of radio pulsars. We find that for a Kolmogorov electron-density turbulence spectrum, TOA perturbations are dominated by dispersion measure variations. Multiple frequency observations remove DM variations to better than one microsecond (~ 0.3 μs in the best simulations). Multiple frequency observations remove the refraction induced TOA variation component with difficulty, since the size of the refractive perturbations scales with frequency. The remaining refraction induced perturbations limit the absolute precision of pulsar timing data dominated by errors in the AOA term.

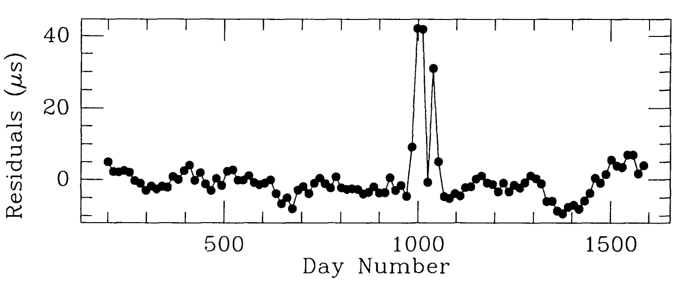

FIG. 10.—Post-fit timing residuals in microseconds are plotted vs. day number showing the effect of a plasma cloud passing between the Earth and the pulsar as observed at 1 GHz. The total change in dispersion measure is 8×10^{-3} pc cm^{-3}.

Observing at the highest possible frequencies probably offers the best solution for avoiding the problem of refraction induced variations in the arrival time data from millisecond pulsars.

A structure-function analysis of the timing residuals can constrain the nature of the electron-density power spectrum. The phase-structure function computed from the single-frequency arrival time residuals in the case of PSR 1937+21 agrees with the expected values from DM fluctuations alone on time scales of 100 to ≤ 300 days. Below 100 days excess power exists in the structure function from nondispersion measure variations in the arrival times. Above 300 days the structure function begins to turn over because the long lags are a large fraction of the entire data set.

With four years of data the simulation easily distinguishes between a Kolmogorov spectrum and other power-law spectrum. The phase-structure functions generated from the simulated data fitted the expected slopes of the original power spectrum. If the real electron-density turbulent spectrum is well approximated by a one-dimensional phase screen model, then long-term uncorrected timing data can provide a measure of the index of an underlying power spectrum. The structure function values for lags greater than ~ 100 days give the best indication of the true spectrum as they are only weakly influenced by short time scales of the refractive perturbations (this time scale is dependent on the source distance, its transverse velocity, and the observing wavelength.)

If discrete scattering events contribute to the timing errors they should show up with very strong frequency dependencies and will contribute excess power to a structure function analysis on scales of order the size of the events. Both the timing data and the structure function analysis can identify or at least place constraints on the amplitude of discrete scattering events. Final residuals of 1 μs at 1 GHz limit the electron-column density fluctuations, in terms of a fractional dispersion measure change, to less than 2.4×10^{-4} pc cm^{-3}.

Frequent sampling of the pulse arrival time data allows for better probing of the electron distribution in the interstellar medium. Comparable timing measurements are obtained with biweekly sampling using a large telescope and daily sampling using a telescope one-half as large, if both are equipped with receivers of the same quality. Frequent sampling provides a better technique for probing the turbulent nature of the electron distribution in the interstellar medium and removing refractive variations from pulsar timing data.

Recent millisecond pulsar surveys (Biggs and Lyne 1990; Fruchter *et al.* 1988; Lyne *et al.* 1987, 1988, 1989, Manchester *et al.* 1989, and Wolszczan *et al.* 1989*a*, *b*) have found low-luminosity objects that are either very weak or invisible at frequencies above 1 GHz. If these objects are to be timed with submicrosecond accuracy, then multiple frequency observations will be needed to remove propagation delays associated with refraction in the interstellar medium or at the very least, place an upper limit on the amplitude of these delays. These results are very sensitive to the particular slope of the electron-density spectrum. Assuming a Kolmogorov turbulence spectrum, low-frequency observations will be strongly influenced by refractive variations, thus limiting the reliability of measuring the pulsar's astrometric parameters of proper motion and parallactic distance.

The authors would like to acknowledge D. C. Backer and R. Romani for their helpful discussions and assistance with the presentation of this material. D. C. Backer originally suggested the importance of examining the influence of angle-of-arrival errors on pulsar timing data. Partial support of this work has come from the National Science Foundation's funding of grants AST-8416863 and AST-8719094 to the University of California at Berkeley and grant AST-8520530 to Cornell University. Additional support provided by the National Astronomy and Ionesphere Center under contract with the National Science Foundation.

REFERENCES

Armstrong, J. W. 1984, *Nature*, **307**, 527.
Biggs, J. D., and Lyne, A. G. 1990, *IAU Circ. No.* **4988**.
Blandford, R. D., Narayan, R., and Romani, R. 1984, *J. Astr. Ap.*, **5**, 369.
Blandford, R. D., and Teukolsky, S. A. 1976, *Ap. J.*, **205**, 580.
Cordes, J. M., Foster, R. S., and Backer, D. C. 1990 in preparation.
Cordes, J. M., Pidwerbetsky, A., and Lovelace, R. V. E. 1986, *Ap. J.*, **310**, 737.
Cordes, J. M., Weisberg, J. M., and Boriakoff, V. 1985, *Ap. J.*, **288**, 221.
Cordes, J. M., Wolszczan, A., Dewey, R. J., Blaskiewicz, M., and Stinebring, D. R. 1990, *Ap. J.*, **349**, 245.
Davis, M. M., Taylor, J. H., Weisberg, J. M., and Backer, D. C. 1985, *Nature*, **315**, 547.
Dewey, R. J., Cordes, J. M., Wolszczan, A., and Weisberg, J. M. 1988, *AIP Proc.*, **174**, 217.
Erickson, W. C., and Mahoney, M. J. 1985, *Ap. J. (Letters)*, **299**, L29.
Fiedler, R., Dennison, B., Johnson, K., and Hewish, A. 1987, *Nature*, **326**, 675.
Foster, R. S., Backer, D. C., Taylor, J. H., and Goss, W. M. 1988, *Ap. J. (Letters)*, **326**, L13.
Foster, R. S., Fairhead, L., and Backer, D. C. 1990, *Ap. J.*, submitted.
Frehlich, R. G. 1988, *AIP Proc.*, **174**, 169.
Fruchter, A. S. 1988, private communication.
Fruchter, A. S., Stinebring, D. R., and Taylor, J. H. 1988, *Nature*, **333**, 237.
Goodman, J., and Narayan, R. 1985, *M.N.R.A.S.*, **214**, 519.
Gwinn, C. R., Cordes, J. M., Bartel, N. H., Wolszczan, A., and Mutel, R. 1988*a*, *AIP Proc.*, **174**, 106.
Gwinn, C. R., Moran, J. M., Reid, M. J., and Schneps, M. H. 1988*b*, *Ap. J.*, **330**, 817.
Heiles, C., Kulkarni, S. R., Stevens, M. A., and Backer, D. C. 1983, *Ap. J. (Letters)*, **273**, L75.
Lee, L. C., and Jokipii, J. R. 1976, *Ap. J.*, **206**, 735.
Lovelace, R. V. E. 1970, Ph.D. thesis, Cornell University.
Lyne, A. G., Biggs, J. D., Brinklow, A., Ashworth, M., and McKenna, J. 1988, *Nature*, **332**, 45.
Lyne, A. G., Brinklow, A., Middleditch, J., Kulkarni, S. R., Backer, D. C., and Clifton, T. R. 1987, *Nature*, **328**, 399.
Lyne, A. G., Johnston, S., Manchester, R. N., Staveleg-Smith, L., D'Amico, N., Lim, J., Fruchter, A. S., and Goss, W. M. 1989, *IAU Circ. No.* **4974**.
Manchester, R. N., Lyne, A. G., Johnston, S., D'Amico, N., Lim, J., and Kniffen, D. A. 1989, *IAU Circ. No.* **4892**.
McKenna, J., and Lyne, A. G. 1988, *Nature*, **336**, 226; **336**, 698.
Rawley, L. A., Taylor, J. H., and Davis, M. M. 1988, *Ap. J.*, **326**, 947.
Rickett, B. J. 1977, *Ann. Rev. Astr. Ap.*, **134**, 390.
Romani, R., Narayan, R., and Blandford, R. D. 1986, *M.N.R.A.S.*, **220**, 19.
Spangler, S. R., and Cordes, J. M. 1988, *AIP Proc.*, **174**, 117.
Taylor, J. H. 1988, private communication.
Taylor, J. H., and Weisberg, J. M. 1989, *Ap. J.*, **345**, 434.
Webbink, R. F. 1985, in *IAU 113, Dynamics of Star Clusters*, ed. J. Goodman and P. Hut (Boston: Kluwer), 541.
Wilkinson, *et al.* 1988, in *IAU 129 The Impact of VLBI in Astrophysics and Geophysics* (Dordrecht: Reidel), 305.
Wolszczan, A., Anderson, S., Kulkarni, S. R., and Prince, T. 1989*a*, *IAU Circ. No.* **4880**.
Wolszczan, A., Kulkarni, S. R., Middleditch, J., Backer, D. C., Fruchter, A. S., and Dewey, R. J. 1989*b*, *Nature*, **337**, 531.

JAMES M. CORDES: Astronomy Department, Space Sciences Building, Cornell University, Ithaca, NY 14853

ROGER S. FOSTER: Astronomy Department, University of California at Berkeley, Berkeley, CA 94720